Synergistic Electro-Catalysis of Pd/PdO Nanoparticles and Cr(III)-Doped $NiCo_2O_4$ Nanofibers in Aprotic Li-O_2 Batteries

Antonio Gentile,[1] Daniela Giacco,[2,z] Angela De Bonis,[1] Roberto Teghil,[1] Andrea Giacomo Marrani,[2] and Sergio Brutti [1,3,*,z]

[1]*Dipartimento di Scienze, Università della Basilicata, 85100 Potenza, Italy*
[2]*Dipartimento di Chimica, Università di Roma La Sapienza, 00185 Rome, Italy*
[3]*ISC-CNR UOS Sapienza, 00185 Rome, Italy*

In this work we discuss the co-catalysis in aprotic Li-O_2 batteries of C-free nanostructured mixed oxide electrodes decorated by Pd/PdO core/shell nanoparticles. A Cr(III) doped $NiCo_2O_4$ material has been grown hydrothermally on an open Ni-mesh. Palladium nanoparticles have been synthesized by pulsed lased ablation in liquid acetone in the fs regime and deposited by drop casting onto the surface of the nanostructured mixed oxide electrodes. The resulting electrodes have been calcined at 300°C. The use of laser techniques to produce nanoparticles for aLOBs is here proposed for the first time in the literature, as well as the peculiar combination of Pd/PdO nanoparticles deposited onto C-free Cr(III) doped $NiCo_2O_4$ self-standing electrodes. Performance in aprotic Li-O_2 batteries have been recorded in galvanostatic conditions and post mortem analysis of the electrode surfaces have been carried out by X-ray photoemission spectroscopy. The use of Pd/PdO nanoparticles as co-catalysts enhances the reversibility of the electrochemical oxygen reduction/evolution reactions. This beneficial effect originates by the decrease of the mean overvoltages compared to the bare Cr(III) doped $NiCo_2O_4$ electrodes, and extends the cell calendar life from 16 to 41 fully reversible galvanostatic cycles at J = 0.2 mAcm^{-2} with capacity limitation of 0.2 mAhcm^{-2}.

 [DOI: 10.1149/2.0081816jes]

Manuscript submitted July 25, 2018; revised manuscript received November 14, 2018. Published November 28, 2018.

Aprotic Li-O_2 batteries (aLOBs) exploit the reversible electrochemical formation/oxidation to O_2 of Li_2O_2 in non-aqueous electrolytes.[1] This redox reaction promises outstanding theoretical performance (e.g. energy density of 3305 Wh kg^{-1}) but its implementation in secondary battery devices still faces fundamental and technological challenges for all the cell constituents (e.g. positive and negative electrodes, electrolytes, gas management system, etc.).[2–4]

Focusing on the positive side, an efficient electrode for aLOBs needs to be: (i) electrically conductive, (ii) porous, (iii) able to accommodate the precipitation/removal of Li_2O_2 particles, (iv) easily wetted by the electrolyte and (v) capable to electro-catalyze both the oxygen reduction reaction (ORR) and the oxygen evolution reaction (OER).[5,6] Moreover it should also be chemically and electrochemically inactive in the highly oxidizing environment of an aLOB, where radicals and strong nucleophilic species can be originated upon cycling.[7,8]

Carbon-based materials are widely used as positive electrodes materials in aLOBs,[9,10] although many authors demonstrated the degradation of the carbonaceous electrode surfaces upon cycling.[11–15] Also transition metal oxides with inverse-spinel structures, like $NiCo_2O_4$, are known as good electro-catalysts for both ORR and OER in aLOBs[16–20] and can be used in C-free self-standing configurations, as demonstrated also by us.[21]

Here we discuss the co-catalysis in aLOBs of a composite C-free self-standing electrode constituted of a $NiCo_2O_4$-based material decorated by Pd/PdO nanoparticles. The use of noble metals as electro-catalysts for ORR and OER is well known.[22–24] As an example, Au and Pt have been successfully used as co-catalysts deposited on C-based electrodes in aLOBd to enhance the performance.[25,26] Recently, the use in aLOBs of Pd nanoparticles as co-catalysts impregnated onto $NiCo_2O_4$ nanosheets/carbon composite electrodes (Pd loading 200 μg cm^{-2}) have been demonstrated by Agyeman et al.,[27] achieving low overvoltages both in ORR and OER, high discharge capacity (i.e. 4000 mAh g^{-1} ≈ 3.2 mAh cm^{-2} at 200 mA g^{-1} ≈ 0.16 mA cm^{-2}) and very good reversibility (100 reversible cycles with 100% coulombic efficiency at 200 mA g^{-1} ≈ 0.16 mA cm^{-2} with capacity limitation of 1000 mAh g^{-1} ≈ 0.8 mAh cm^{-2}).

In this work we demonstrate the synergistic co-catalysis in aLOBs of composite C-free electro-catalysts constituted by a nanostructured porous Cr(III) doped $NiCo_2O_4$ material decorated by Pd/PdO nanoparticles (Pd/PdO-NP). The palladium-based nanoparticles have been produced by pulsed lased ablation in liquid acetone (PLAL) in the fs regime, deposited by drop casting from an acetone suspension onto the surface of the mixed oxide self-standing electrodes and calcined at 300°C. PLAL is an emerging bottom-up approach widely used to synthesize nanomaterials with controlled structures and morphologies.[28] In fact nanomaterials properties can be easily tuned in PLAL by an appropriate combination of solvents, additives and targets,[29] thus making this technique a versatile environmentally friendly route to synthesize innovative materials.[28] The use of PLAL to produce nanoparticles for aLOBs is here proposed for the first time in the literature, as well as the peculiar combination of Pd/PdO nanoparticles deposited onto C-free Cr(III) doped $NiCo_2O_4$ self-standing electrodes. All materials have been characterized by X-ray diffraction, scanning electron microscopy (SEM) coupled with energy dispersive spectroscopy (EDS), transmission electron microscopy (TEM) and X-ray photoemission spectroscopy (XPS). Performance in aLOBs have been recorded in galvanostatic conditions and post mortem analysis of the electrode surfaces have been carried out by XPS in order to shed light on the origin of the de-activation of the electro-catalysts.

Experimental

Bare Cr(III)-doped $NiCo_2O_4$ (NCCr@Ni samples) was grown on a nickel mesh by means of the hydrothermal method discussed by us in Ref. 21. Prior to the synthesis procedure, the Ni was punched into disks with a diameter of 14 mm. Approximately, the cobaltite loading on each disk was ∼1 mg cm^{-2}.

A suspension of metallic palladium nanoparticles in acetone was prepared by means of pulsed lased ablation in liquid (PLAL) using a pulsed laser Ti:Sapphire Spectra Physics – Spitfire following a procedure optimized by us previously.[30,31] The pulse duration was 120 fs with a repetition rate of 1 KHz. The laser fundamental wavelength

*Electrochemical Society Member.
[z]E-mail: daniela.giacco@uniroma1.it; sergio.brutti@unibas.it

was 800 nm and the spot on the Pd target was 10^{-3} cm^2, so the fluence was 3.5 J cm^{-2}. Approximately, the resulting concentration of the NP in acetone was 100 μg mL^{-1}.

NCCr@Ni samples were decorated with Pd/PdO-NPs (Pd/PdO@NCCr@Ni samples) by drop casting of 1 mL of palladium nanoparticle acetone suspension on their surface. The Pd/PdO@NCCr@Ni electrodes were finally calcined at 300°C for 4 h in air. Approximately, the Pd/PdO-NPs loading on the cobaltite was 66 μg cm^{-2}.

For the sake of completeness, the Pd/PdO-NPs were also deposited directly by drop casting on the clean Ni mesh (Pd/PdO@Ni samples) with an identical loading (66 μg cm^{-2}) compared to the Pd/PdO@NCCr@Ni sample and calcined at 300°C.

The XRD experiments were carried out using a Siemens D5000 diffractometer equipped with a CuKα source and a graphite monochromator for the diffracted beam. XP spectra were recorded using a modified Omicron NanoTechnology MXPS system equipped with a monochromatic X-ray source (Omicron XM-1000) and an Omicron EA-127 energy analyzer. The exciting radiation was Al Kα ($h\upsilon$ = 1486.7 eV), generated operating the anode at 14–15 kV and 10–20 mA. The experimental spectra were reconstructed by fitting the secondary electrons' background to a Shirley function and the elastic peaks to pseudo-Voigt functions described by a common set of parameters (position, FWHM, Gaussian-Lorentzian ratio) free to vary within narrow limits. During the fitting procedures the Gaussian-Lorentzian ratio was left free to vary between 0.6 and 0.9. The C 1s binding energy (BE) of the -CH_2- groups at 284.8 eV belonging to the aliphatic carbon contamination on the cathodes surface was used as an internal standard reference for the BE scale (accuracy of ±0.05 eV). Field Emission-SEM experiments (FESEM) were carried out by a Zeiss Auriga electron microscope equipped with a field emission source and a Bruker energy dispersive X-ray spectroscopy (EDS) probe. SEM experiments were carried out by a PHILIPS-FEI XL 30 ESEM instrument equipped with an EDS probe. TEM analysis was carried out using a FEI Tecnai 200 kV cryo-TEM instrument. TEM pictures have been analyzed using the ImageJ software.[32]

Li-O_2 electrochemical cells preparation was realized in a Iteco Engineering argon-filled glove box using ECC-AIR cells by EL-CELL: a metallic lithium coin was coupled with (i) a glass-fiber separator (Whatman) impregnated with 150 μL cm^{-2} of a non-aqueous electrolyte and (ii) a positive porous electrode. The electrolyte was a 1 molal solution of LiTFSI dissolved in TEGDME (Sigma-Aldrich, moisture controlled grade). The ~3 cm^3 dead-volume above the positive electrode was filled with an overpressure of O_2 (5.0 purity). The starting oxygen partial pressure was 1.0 bar. Electrochemical tests were carried out by using a MTI Corp. battery cycler: currents regimes were set in terms of current densities (J) by dividing for the geometrical area of the cathodes (1.54 cm^2). Galvanostatic cycling of the cells were carried out, connecting them to a MTI Corp. battery cycler imposing a current density of 0.05 mA cm^{-2} and cutoff voltages of 2.0 V and 4.1 V in discharge and charge, respectively. The measured capacity was normalized dividing by the geometrical area of electrode. A pseudo-Tafel plot has been derived from intermitted galvanostatic titrations experiments performed at various current densities. Electrodes have been partially pre-discharged with a voltage cutoff fixed at 2.6 V vs. Li at 0.025 mA cm^{-2} and then, after 12 h of relaxation in open circuit conditions (OCV), a constant current density signal (J) has been applied followed by 6 h of cell relaxation in OCV. Nine J values have been sampled both in ORR and OER (±1.3, ±3.3, ±6.5, ±13, ±32.5, ±65, ±130, ±325, ±650 μA cm^{-2}, respectively) by partially discharging/charging the electrodes with a capacity limitation of ±0.01 mAh cm^{-2}, in order to restore after each polarization the starting electrode composition. In a third set of experiments, the cells were galvanostatically discharged/charged with a capacity limit of 0.2 mAh cm^{-2} at a current density value of 0.2 mA cm^{-2}. After the electrochemical tests, the cells were disassembled in an argon-filled glove box. The post-mortem electrodes were recuperated and washed in TEGDME and in THF to remove the excess electrolyte, and dried under vacuum at room temperature. Recuperated cathodes were characterized by XPS.

Results and Discussion

Characterization of the pristine materials.—The physico-chemical characterization of the palladium nanoparticles synthesized by PLAL before the deposition onto to the mixed oxide electrodes is shown in Figure 1. The diffraction pattern (Figure 1a) shows the expected peaks for metallic Pd (JCPDS Card No. 01-087-0637). From the morphological point of view, FE-SEM and TEM images (Figures 1b–1d) highlight the formation of rounded nanoparticles polydispersed in size. The mean nanoparticle diameter has been estimated by the TEM picture analysis and falls in the range 10–30 nm. These palladium nanoparticles are highly crystalline as nicely demonstrated by the indexing of the electron diffraction pattern in the [111] zone derived by the selected area Fast-Fourier-Transform (FFT) of the Figure 1d.[30,33,34]

Turning to the mixed oxide self-standing materials, a full characterization of the bare NCCr@Ni sample has been reported by us in Ref. 21 and additional comments would be redundant: here we illustrate and discuss in detail the analysis on the Pd/PdO@NCCr@Ni material in comparison with the bare one.

The palladium nanoparticle suspension has been dispersed onto the NCCr@Ni porous electrodes: the comparison between the morphology of the bare and Pd/PdO@NCCr@Ni electrodes obtained after calcination is shown in Figures 2a–2b. Whereas the NCCr@Ni surface is constituted by well separated oxide-based polycrystalline fibers, the Pd/PdO@NCCr@Ni material shows a partial aggregation of the polycrystalline oxide nanowires and accumulation of round particles among the 1D nanostructures. Therefore the resulting surface morphology of the Pd/PdO@NCCr@Ni electrodes is qualitatively more compact with less voids compared to the bare one.

As expected, the XRD pattern for Pd/PdO@NCCr@Ni (Figure 2c) shows, the peaks of a cubic $NiCo_2O_4$ phase (JCPDS Card No. 73-1702).[35] Additional reflections can be assigned to the Ni mesh (JCPDS Card No. 04-0850),[36] to traces of NiO (JCPDS Card No. 73-1523)[37] grown from the Ni mesh due to the spontaneous corrosion in alkaline aqueous solutions[38] and to metallic Pd (JCPDS Card No. 01-087-0637).[36] The EDS analysis performed on the area of the samples shown in the FE-SEM picture in Figures 2d, 2e, 2f confirms the homogeneous distributions of both the Cr^{3+}dopant and the Pd co-catalyst on the cobaltite nanowires.

The Ni $2p_{3/2}$, Co $2p_{3/2}$ and Cr 2p XP spectra of the Pd/PdO@NCCr@Ni material are shown in Figures 3a, 3b and 3c respectively. The profiles of the signals are fully compatible with already reported data on cobaltite-type compounds[39,40] and with those reported by us previously for the NCCr@Ni bare material.[21]

The Ni $2p_{3/2}$ photoionization region (Figure 3a) has been theoretically reconstructed by means of a peak-fitting procedure using six components. Their absolute positions and relative Binding Energy (B.E.) distances are in agreement to those reported for NiO samples.[41,42] The fitting parameters and the attributions of the signals to different final ionized states of Ni(II) centers, as well as for the Co states (see below for the discussion) are reported in Table 1.

Besides the expected component at 854.7 eV due to the Ni(II) ions in cubic oxides,[43,44] it is remarkable to observe a component centered 856.3 eV. In NiO this feature has been widely accepted to be related to the d^8:cd^9L final ionized states of Ni(II) sites[43,44] whereas, in spinel phases, its attribution to Ni(III) centers has been proposed by many authors.[39,45] This peak reconstruction matches the one reported by us for the NCCr@Ni sample [21]. Overall, the analysis of the Ni 2p region suggests that the deposition of the Pd NP and the subsequent calcination leave unaltered the ratio of the Ni(II)/Ni(III) centers over the surface of the Pd/PdO@NCCr@Ni material compared to the bare one.

A similar picture is also observed in the Co $2p_{3/2}$ photoionization region (Figure 3b), where the absolute position and the relative B.E. distances of the peaks are analogue to those for mixed-valence cobalt

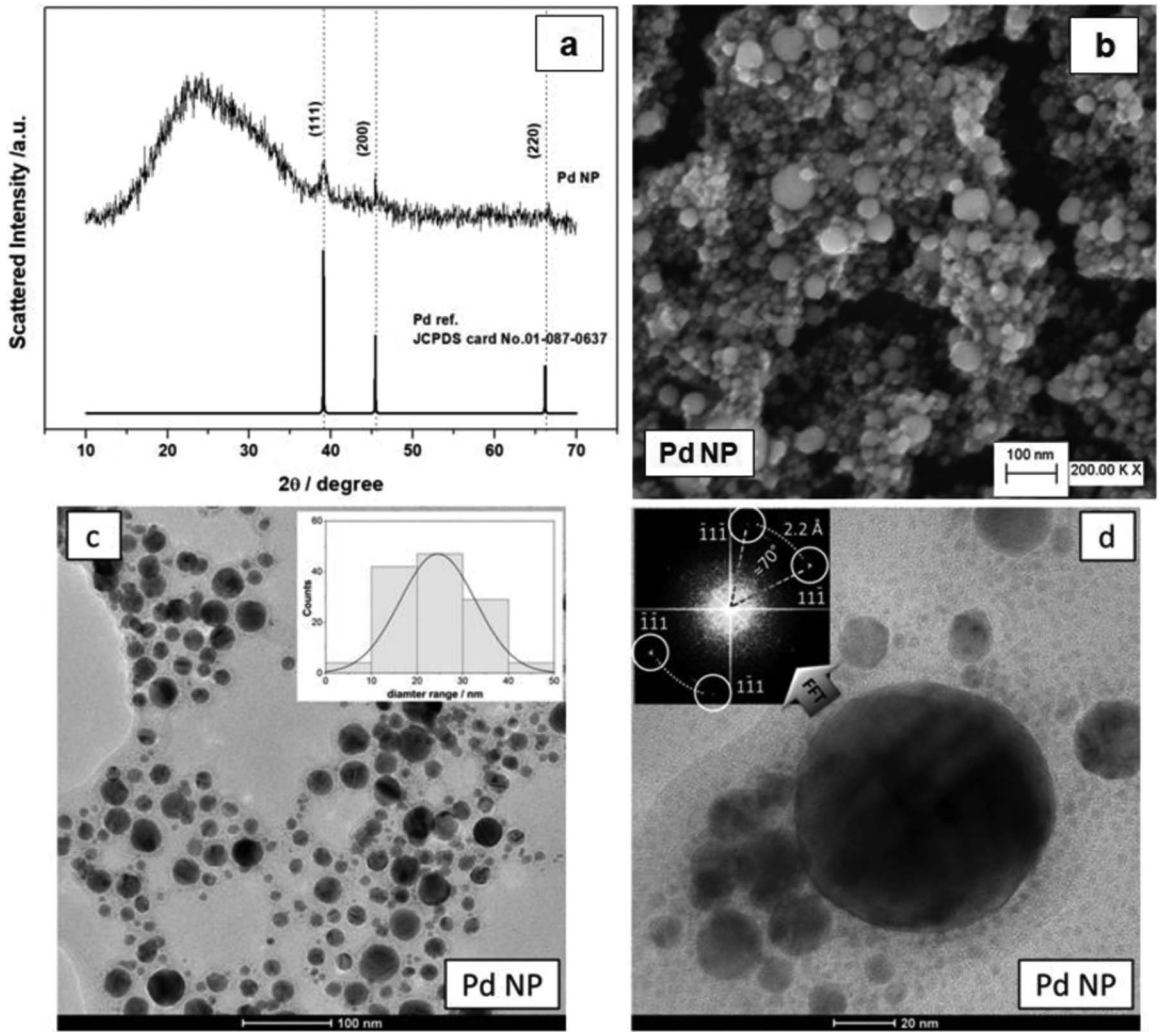

Figure 1. (a) Diffraction patterns of the Pd nanoparticles accumulated onto a silicon wafer from the acetone suspension compared to the reference; (b) morphology of the Pd nanoparticles by FE-SEM; (c-d) TEM pictures at different magnifications of the palladium nanoparticles (1c inset: particle size distribution; 1d inset: FFT analysis of the Pd NP corresponding to a diffraction pattern in [111]).

oxides (i.e. Co_3O_4 samples)[39,46] and in good agreement with those previously reported by us for NCCr@Ni samples [21]. Therefore, as for the bare material, in the case of the Pd decorated one, the co-presence of Co(II) and Co(III) ions in the $NiCo_2O_4$ spinel lattice is confirmed. Moreover, the low intensity of the peak located at 785.2 eV, related to a shake-up satellite of Co(II) sites, is compatible with a Co(II) predominance in tetrahedral sites.[39]

Table I. B.E. position and assignments for the peaks determined after curve fitting of the experimental Ni $2p_{3/2}$ and Co $2p_{3/2}$ spectra of the Pd/PdO@NCCr@Ni pristine material.

Peak	B.E. position (eV)	Assignments
Ni $2p_{3/2}$	854.7	cd^9L
	856.3	d^8:cd^9L
	857.5	cd^9:d^7 non-local screening
	861.8	$cd^{10}L^2$
	865.0	cd^8
	867.2	shake-up satellite
Co $2p_{3/2}$	779.6	Co^{3+} cd^7L
	780.9	Co^{2+} cd^8L
	782.2	$Co^{2+}cd^9L^2$
	785.2	$Co^{2+}cd^7$ (shake-up satellite)
	789.5	Co^{3+} cd^7 (shake-up satellite)

A full reconstruction of the Cr 2p photoemission region (Figure 3c) was not attempted due to a too low signal-to-noise ratio. However, the position (575–579 eV for the $2p_{3/2}$ peak) of the spin–orbit components, broadened due to multiplet splitting, is compatible with the incorporation of Cr(III) ions within the cobaltite spinel lattice.[46]

The comparison between the Pd 3d XP spectra of the palladium nanoparticles deposited on a silicon wafer directly from the acetone suspension (lower spectrum, no calcination at 300°C) and the Pd/PdO@NCCr@Ni sample (upper spectrum) is shown in Figure 3d. The absolute positions (i.e. about 335.4 eV and 337.4 eV for the $3d_{5/2}$ peaks, respectively) and the spin-orbit coupling separation (i.e. 5.4 eV and 5.2 eV, respectively) of the peaks are in good agreement with those reported for Pd and PdO samples for the pristine palladium nanoparticles and the Pd/PdO@NCCr@Ni sample, respectively.[47,48] Therefore XPS results highlight the presence of a layer of metal oxide, few nanometers thick, on the palladium nanoparticles surface on the Pd/PdO@NCCr@Ni sample whereas the pristine nanoparticle surface was purely metallic. Apparently, after the dispersion onto the mixed oxide substrate, the outer layers of the palladium nanoparticles oxidize, likely during the calcination at 300°C. Being the core structure of the nanoparticles after deposition/calcination still constituted by metallic Pd (see Figures 1a and 2c), the resulting co-catalyst dispersed onto the surface of the Pd/PdO@NCCr@Ni samples is therefore constituted by Pd/PdO nanoparticles, likely with a core-shell nano-morphology.

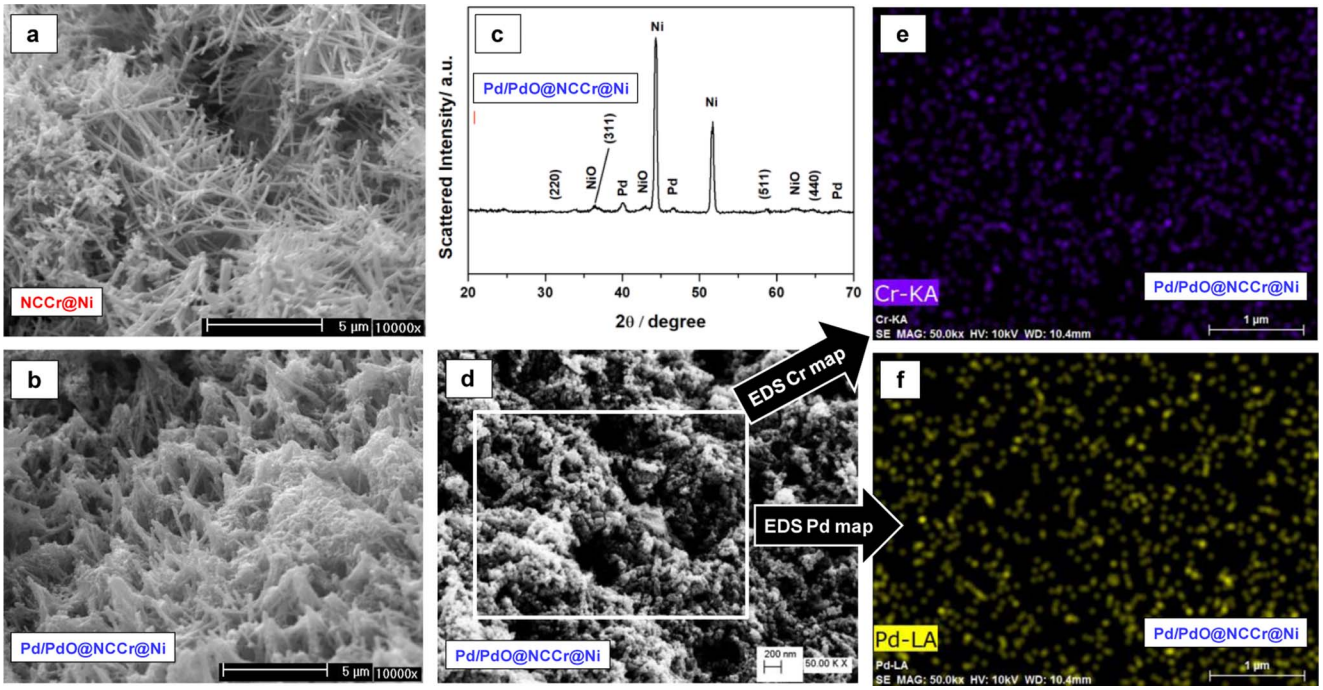

Figure 2. SEM picture of (a) the NCCr@Ni sample compared to (b) the Pd/PdO@NCCr@Ni one. (c) Diffraction pattern and (d-e-f) surface analysis by SEM/EDS maps (Cr-Kα and the Pd-Lα emissions of the area highlighted) of the Pd/PdO@NCCr@Ni sample. In the Figure 2c the (hkl) labels refer to the cobaltite spinel lattice peak indexing, whereas reflections due to the other constituents (i.e. Pd and NiO) are explicitly assigned.

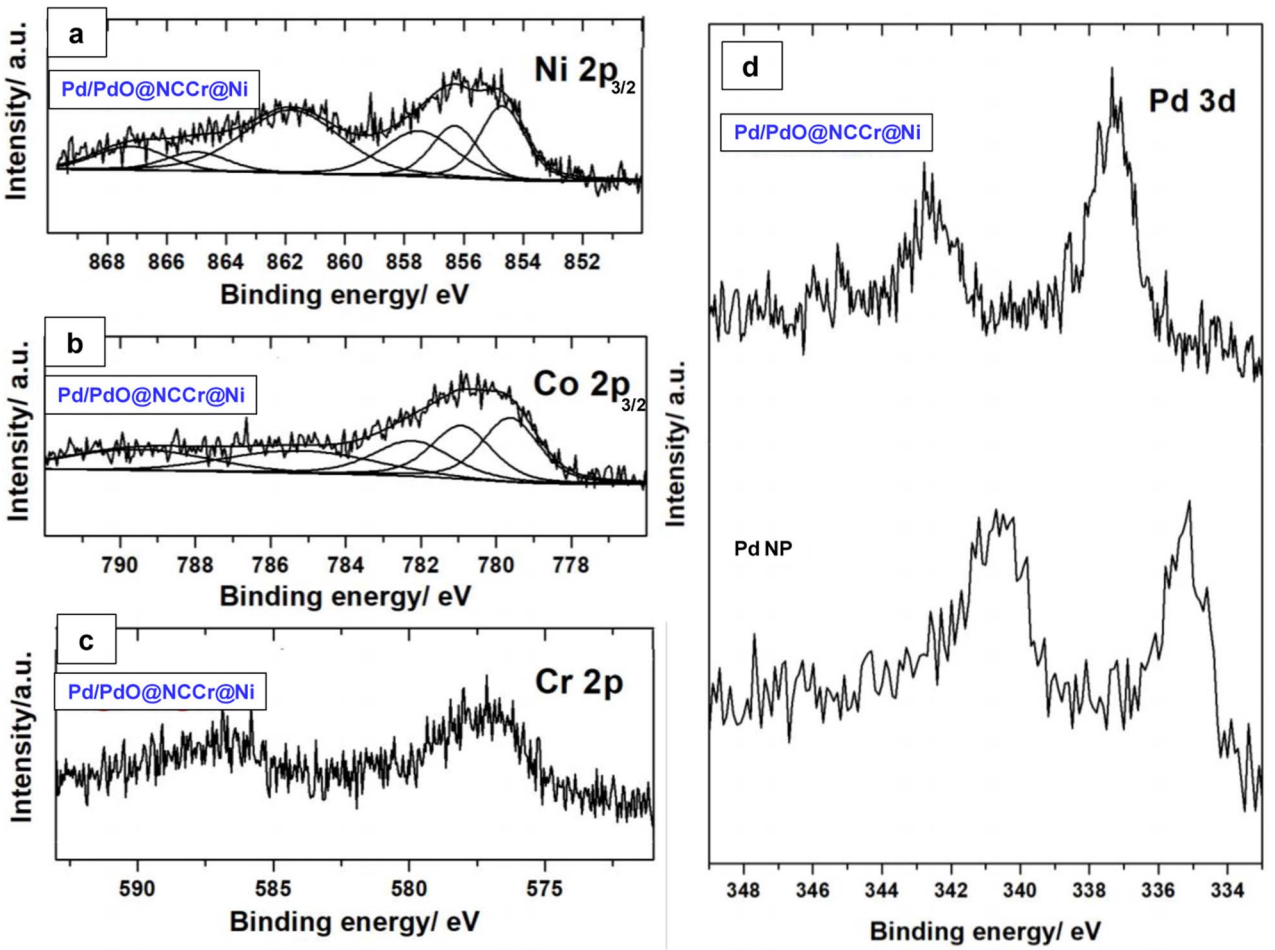

Figure 3. (a) Ni $2p_{3/2}$, (b) Co $2p_{3/2}$, (c) Cr 2p and (d) Pd 3d regions of the XP spectra for the Pd/PdO@NCCr@Ni sample. In (d) the Pd 3d region is also shown for the Pd NP.

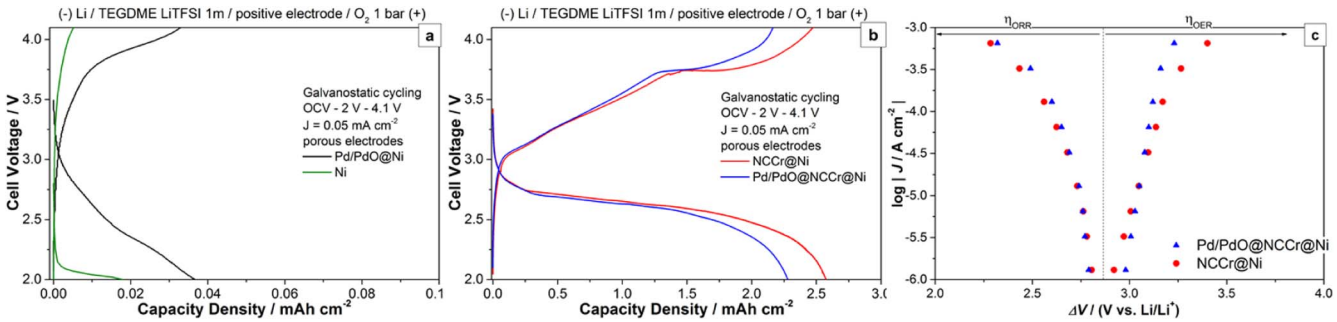

Figure 4. Electrochemical properties of the various positive electrode materials. Galvanostatic discharge and charge (first cycle) at J = 0.05 mA cm^{-2} for Li-O_2 electrochemical cells: comparison among (a) the nickel foam and the Pd/PdO@Ni, (b) the NCCr@Ni and the Pd/PdO@NCCr@Ni porous electrodes. (c) Current densities (*J*) versus discharge/charge working potential measured on the NCCr@Ni and the Pd/PdO@NCCr@Ni electrodes pre-discharged at 2.6 V with a J = 0.025 $mAcm^{-2}$.

Electrochemical activity in aLOBs.—The performance of the porous C-free electrodes in aLOBs are compared in Figures 4a–4b. At J = 0.05 mA cm^{-2}, the Pd/PdO@NCCr@Ni electrode almost matches the discharge capacity of the NCCr@Ni one (2.28 mAh cm^{-2} vs. 2.60 mAh cm^{-2} for the Pd/PdO@NCCr@Ni and NCCr@Ni electrodes, respectively, corresponding to approximately 2300–2600 mAh g^{-1}) as well as the charge capacity and the mean operating voltages.

The obtained areal capacity values for the Pd/PdO@NCCr@Ni electrode are in reasonable agreement with the findings of Agyeman et al.[27] on (Pd impregnated/$NiCo_2O_4$ nanosheets/carbon) electrodes (meallic Pd loading 200 μg cm^{-2}, performance in aLOB ≈ 3.2 mAh cm^{-2} at ≈ 0.16 mA cm^{-2}). The larger capacity values measured by Agyeman et al.[27] compared to ours may be due to: (a) the more efficient electro-catalytic effect provided by the clean Pd nanoparticles free from any PdO coating; (b) the larger areal noble metal nanoparticle concentration, and (c) the more efficient gas transport through the carbon-based gas-diffusion layer compared to the open Ni-mesh.

For the sake of completeness, the performance of the nickel foam and the Pd/PdO@Ni electrodes have been also recorded to decouple the net electro-catalytic effect supplied by the palladium nanoparticles and the contribution of the nickel support. Both the nickel foam and the Pd/PdO@Ni electrodes show negligible performances in aLOBs. This evidence suggests an essential key-role played by the mixed oxide in the electro-catalysis and an apparent marginal promotion of the ORR/OER by the unsupported Pd/PdO nanoparticles.

In order to shed more light in the role of the palladium nanoparticles deposited on the nanostructure cobaltite on the performance in aLObs, we also studied the evolution of the ORR and OER working voltages as shown in the pseudo-Tafel plot in Figure 4c for the Pd/PdO@NCCr@Ni electrodes compared to the bare NCCr@Ni ones. Both materials show very similar overvoltages in discharge (η_{ORR}) at small current densities, whereas at J > 0.1 mA cm^{-2} the Pd/PdO@NCCr@Ni electrode outperform the bare NCCr@Ni one. Upon charge a similar trend is observed as the Pd/PdO@NCCr@Ni electrodes show smaller overvoltages (η_{OER}) at J > 0.05 mA cm^{-2}. This trend can be a clue of an improvement of the electro-catalysis induced by the simultaneous presence palladium nanoparticles and the of Cr(III) doped mixed oxide. On the other hand the improvement in the electro-catalysis may also originate from different specific surface area of the two different electrodes arising from additional small voids/pores due to the nanometric Pd/PdO particles. A quantification of this effect is unfortunately beyond our experimental capabilities. However it is important to recall that besides the possible synergistic electro-catalysis of the Pd/PdO nanoparticles and the mixed oxide, a different specific surface area might indeed bring to different specific currents and, hence, different overvoltages.

The occurrence of the ORR/OER reactions has been checked by XPS on both post mortem NCCr@Ni and Pd/PdO@NCCr@Ni samples recuperated at the end of discharge (at 2.0 V; J = 0.05 mA cm^{-2}) and after 1 full cycle. The Li 1s spectral region is shown in Figure 5. On discharge (i.e. D.2.0V samples) we observe for both samples the appearance of the characteristic signals for lithium oxide species.[49] This weak XP signals possibly attributed to Li_2O_2 is in line with previous literature reports (see as an example Refs. 14,15,24). In order to support the XPS evidence of the precipitation of Li_2O_2 we also tried ex situ XRD and Raman spectroscopy. Both these techniques failed in a more conclusive detection, likely due to the amorphous nature of the Li_2O_2 phase driven by the surface mediated precipitation mechanism and the need for protective layers (Kapton film or sapphire window for XRD and Raman respectively). A possible alternative test to quantify the Li_2O_2 production is the so-called "$TiOSO_4$-test", adapted and used in aLOBs by Bruce et al.[50] or Gasteiger et al.[51] in recent works. Unfortunately this analytical test requires instrumentation beyond the capability of our laboratory.

After 1 full cycle (i.e. 1 cycle sample), in the case of the Pd/PdO@NCCr@Ni material, the Li 1s signals likely attributed to lithium oxide species completely disappear, whereas a minimal signal is possibly detected for the NCCr@Ni one. Although speculative, this finding may be a clue of an enhancement of the electro-catalysis in the OER provided by the composite electrode decorated with noble metal particles in respect to that of the bare mixed oxide.

The cycling performance in galvanostatic tests with limited capacity cutoff are shown in Figure 6. At J = 0.2 mA cm^{-2}, the capacity limitation of 0.2 mAh cm^{-2} is successfully reached with a coulombic efficiency of 100% between charge and discharge for 40 cycles in the case of the Pd/PdO@NCCr@Ni material, whereas the NCCr@Ni electrode fails at cycle 16. Thus, the presence of the Pd/PdO nanoparticles enhances the reversibility of the ORR/OER reactions.

The evolution of the voltage profiles upon cycling is shown in Figures 6b and 6c. It is remarkable to observe that the Pd/PdO@NCCr@Ni electrodes show smaller overvoltages upon cycling compared to the bare ones. The values and trends of the discharge (ORR) and charge (OER) mean voltages for the Pd/PdO@NCCr@Ni and NCCr@Ni electrodes are compared in Figures 6d and 6e, respectively, and the corresponding voltage hysteresis is shown in Figure 6f.

The mean cell voltage in discharge upon cycling is higher for the Pd/PdO@NCCr@Ni electrodes compared to the NCCr@Ni of approximately ~0.18 V due to the smaller ORR overvoltages. The same trend is observed also upon charge where the mean operating voltages for the Pd/PdO@NCCr@Ni material is ~0.14 V smaller compared to the NCCr@Ni one, thanks to the smaller OER overvoltages.

These combined beneficial effects provided by the Pd/PdO nanoparticles lead to a smaller voltage hysteresis of approximately 0.30–0.35 V between discharge and charge, thus increasing the overall energy efficiency of ~20%. In particular, the surface energy densities in discharge at cycle 10 are 0.556 mWh cm^{-2} and 0.518 mWh cm^{-2} (~550 and 520 Wh kg^{-1}) with an energy efficiency between charge

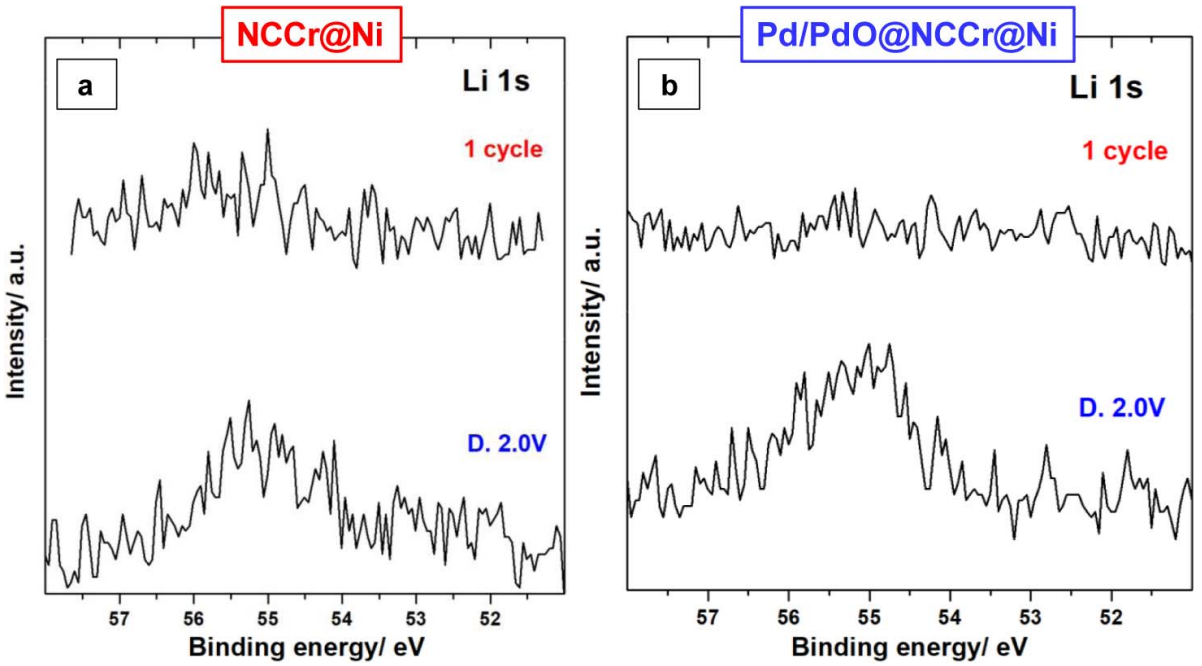

Figure 5. (a,b) Li 1s X-ray photoemission region of the NCCr@Ni and Pd/PdO@NCCr@Ni porous post mortem electrodes recuperated after galvanostatic cycling at J = 0.05 mA cm^{-2}: end of discharge at 2.0V (ORR) and after a full discharge/charge cycle (ORR & OER) at 4.1V.

and discharge of 72% and 66% for the and NCCr@Ni electrodes, respectively.

Turning to the cell failure, it occurs for both materials during the discharge stage due to an increase of the ORR overvoltages cycle-by-cycle. Generally speaking the increase of the overvoltages upon cycling in aLOBs is due to the passivation of the electro-catalyst by the accumulation of solvent degradation by-products over the positive electrode.[15] In this view, the longer cycling life observed for the Pd/PdO@NCCr@Ni sample in respect to the bare one is an evidence of the possible delayed de-activation of electro-catalyst surface due to a mitigation of the solvent degradation reactions. An alternative interpretation of the enhancement of the cell life with the Pd/PdO@NCCr@Ni electrodes may imply the mitigation of the de-activation of the lithium metal negative electrode. Lithium metal negative electrodes are in fact a remarkable limiting factor in aLOBs.[1] Our experimental evidences do not allow to decouple these effects and thus our interpretation call for a general enhancement of the electrochemical stability of the overall formulation.

Ex-situ C 1s XPS regions after cell death.—The C 1s photoemission regions registered ex-situ for the NCCr@Ni and Pd/PdO@NCCr@Ni electrodes recuperated at the cell death (i.e. galvanostatic cycling between 2.0V and 4.6V at J = 0.2 mA cm^{-2}) are shown in Figure 7.

For both samples, we observe a signal for aliphatic carbon (284.8 eV)[46] and the characteristic peaks for the solvent TEGDME (286.1-286.5 eV)[14] and the $–CF_3$ groups of the LiTFSI salt (292.3–292.7 eV).[15] Besides these components, also an additional signal due

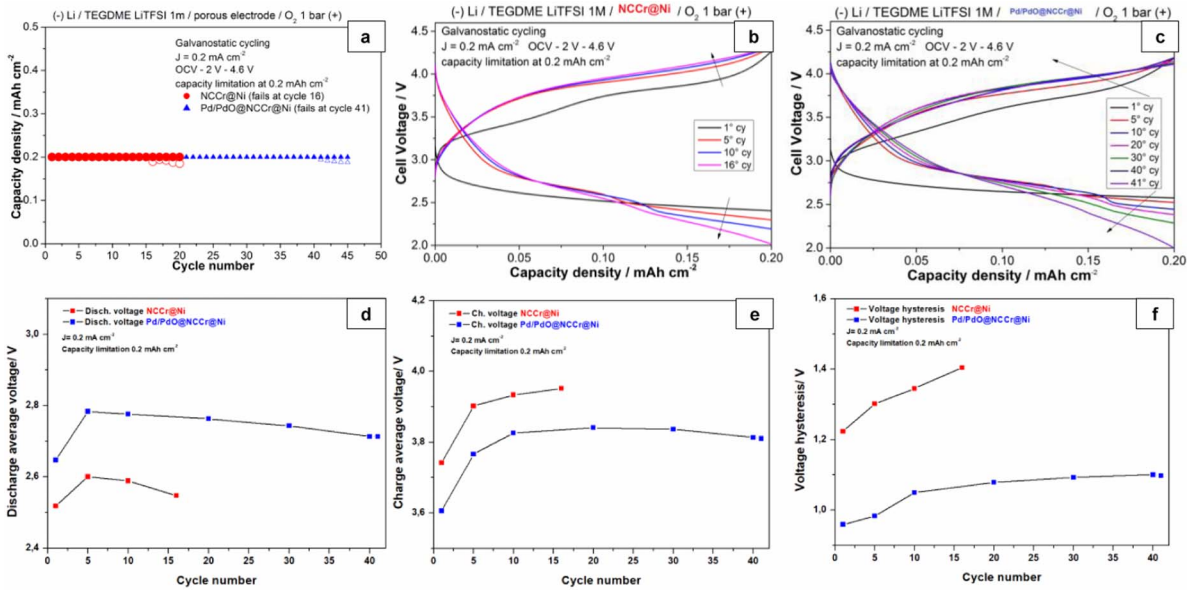

Figure 6. Performance in limited capacity galvanostatic cycling for the NCCr@Ni and Pd/PdO@NCCr@Ni porous electrodes: (a) capacity density and cell failure; (b-c) cell voltage profiles upon cycling; (d-e) mean discharge/charge voltages; (f) voltage hysteresis.

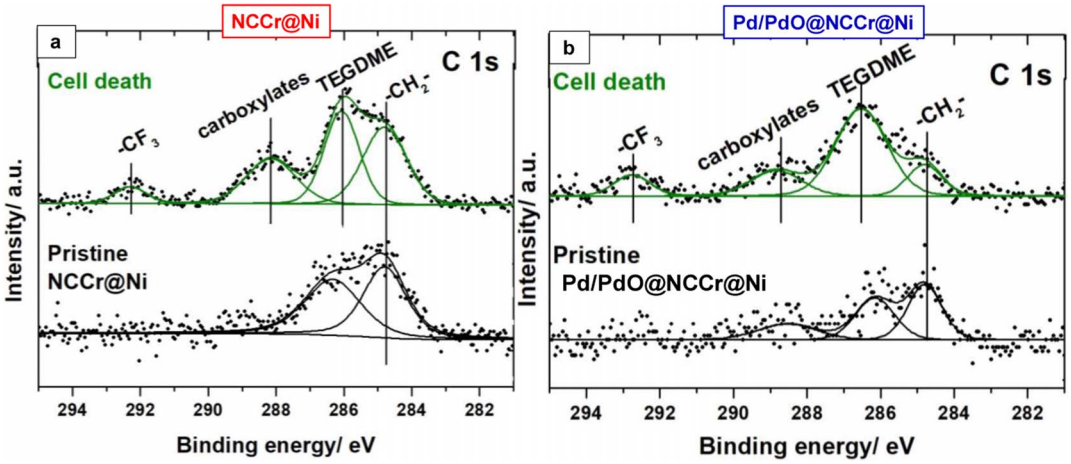

Figure 7. (a,b) C 1s X-ray photoemission regions of the NCCr@Ni and Pd/PdO@NCCr@Ni porous electrodes at the cell death after galvanostatic cycling between 2.0V and 4.6V at J = 0.2 mA cm^{-2} with a capacity limitation of 0.2 mAh cm^{-2}.

to carboxylates is visible in both samples (288.1–288.5 eV).[24,52] As reported previously, these species grow on the electrode surface due to the TEGDME degradation initiated by highly reactive oxygenated species (i.e. O_2^-, O_2^{2-}, $^1O_2$, LiO_2, Li_2O_2),[7,24,53] and passivates the electrode surface.

The most remarkable difference between the bare and the Pd/PdO@NCCr@Ni sample is an enlargement of the TEGDME peak for the Pd/PdO-decorated porous electrode and a slightly less intense carboxylate signal. Generally speaking an XPS component with a large full-width-half-maximum can hide unresolved signals. In our case we may speculate about additional components related to other less-oxidized degradation by-products (e.g. polyethers, epoxides etc.) grown onto the the Pd/PdO@NCCr@Ni sample.

This picture is confirmed by the evolution of the signals in the metals characteristic photoemission regions (i.e. Ni 2p, Co 2p, Cr 2p and Pd 3d, data not shown) that are sensibly attenuated after cycling, particularly in the case of the NCCr@Ni one. In fact the fitted Ni/C and Co/C atomic ratios remarkably decrease between pristine material and those recuperated at the cell death of about 85% and 48% for the NCCr@Ni and the Pd/PdO@NCCr@Ni materials, respectively. This finding calls for the formation of a thinner organic layer on the Pd/PdO decorated porous electrodes in agreement with the moderately lower intensity of the carboxylates.

Overall, on both electrodes a chemically similar organic film constituted by degradation products grows cycle-by-cycle likely trapping LiTFSI and solvent molecules. This organic composite film passivates the metallic catalytic centers of both the porous material, thus leading to a progressive deterioration of the electro-catalytic properties and to the cell death. The improved calendar life recorded for the Pd/PdO@NCCr@Ni sample suggests that the composite electro-catalyst is less active in the promotion of electro-active parasitic reactions. Our interpretation is that the co-presence of Pd/PdO NPs and the Cr-doped $NiCo_2O_4$ electro-catalysts enhances the selectivity toward ORR and OER, thus limiting the parasitic chemistry thus preserving the electroactive sites on the positive electrode surface and/or mitigating the de-activation of the lithium metal electrode.

The analysis of the degradation chemistry in the aLOBs is a very complex topic.[1,7,14,15,24] Generally speaking parasitic by-products forms in aLObs upon discharge due to the chemical attack of LiO_2 and $^1O_2$ toward the solvent molecules, as demonstrated by many authors (see Refs. 1,7,11,14,15,24,51). Upon charge the degradation chemistry is less clear and it is likely initiated by the release of $^1O_2$ by the oxidation of Li_2O_2 at large overvoltages.[52] Our experimental approach does not allow for a detailed analysis of these reactions. However some speculations can be drawn.

LiO_2 is a very strong nucleophilic radical molecule[7] and it is an unavoidable intermediate in ORR ($O_2+Li^++e^-\rightarrow LiO_2$).[1,11] Once formed LiO_2 may: (a-b) dimerize/decompose by releasing Li_2O_2 and O_2 (either in the (a) singlet or (b) triplet states);[11,54] (c) be further reduced[1] to give Li_2O_2; (d) attack the solvent molecules to give $HLiO_2$ and organic alkyl radicals.[7] The competition among these reactions is driven by the corresponding kinetics constants, that may be altered by catalysts. A similar analysis is possible also for the $^1O_2$ molecule. Once formed $^1O_2$ may (e) be quenched[51] to the triplet state, i.e. $^3O_2$, or (f) attack the solvent molecules to form peroxides or other oxidized by-products.[24] Also in this second case the presence of a catalyst may alter the competition between these reactive channels. The better ORR/OER selectivity of the Pd/PdO-decorated mixed oxide catalyst may be originated by an alteration of the kinetics of some of these reactions. In particular one may further speculate that the presence of the Pd/PdO nanoparticles may enhance the kinetics of reactions (b-e), reduce the charge transfer resistance of reaction (c), hinder reactions (a-d-f) or increase the charge transfer resistance of $Li_2O_2\rightarrow 2Li^++2e^-+{}^1O_2$ (see Refs. 54 and 55). Computational modelling of the various reactions performed in proximity of different surfaces (mixed oxide or PdO) may help to clarify at atomic level the origin of the better selectivity of the Pd/PdO-decorated mixed oxide catalyst compared to the bare one.

Conclusions

In this work we discussed the physico-chemical properties and performance as positive electrode in aLOBs of a C-free nanostructured oxide material decorated with Pd/PdO nanoparticles. Palladium nanoparticles have been synthesized by pulsed lased ablation in liquid acetone in the fs regime, deposited by drop casting onto the surface of the nanostructured mixed oxide electrodes and then calcined at 300°C. The use of laser techniques to produce nanoparticles for aLOBs is here proposed for the first time in the literature, as well as the peculiar combination of Pd/PdO nanoparticles deposited onto C-free Cr(III) doped $NiCo_2O_4$ self-standing electrodes.

The electrochemical tests in aLOBs demonstrated the synergistic co-catalysis provided by the Pd/PdO nanoparticles and the Cr(III)-doped $NiCo_2O_4$ in the ORR/OER. This beneficial effect enhances the calendar life of the Pd@NCCr@Ni electro-catalyst in respect to the bare NCCr@Ni-based one. Moreover post-mortem characterizations of the electrodes recuperated from the dead cells suggest an increased selectivity toward ORR/OER of the Pd/PdO decorated electrodes that are able to mitigate the degradation of the TEGDME upon cycling.

Overall our study reports for the first time in the literature the synthesis, characterization and electrochemical tests of a new innovative nanostructured composite material produced with a synthesis route (LAL) never explored so far for aLOBs applications.

Acknowledgments

DG acknowledge the University of Basilicata for the hospitality during her research stage. AGM thank the University of Rome "La Sapienza" for financial support through the Ateneo Project 2015 (C26A152T5M). SB thank the University of Basilicata for the funding through the RIL 2015 grant.

ORCID

Sergio Brutti https://orcid.org/0000-0001-8853-9710

References

1. N. Mahne, O. Fontaine, M. Ottakam Thotiyl, M. Wilkening, and S. Freunberger, *Chem. Sci.*, **8**, 6716 (2017).
2. K. Song, D. A. Agyeman, M. Park, J. Yang, and Y.-M. Kang, *Adv. Mater.*, **29**, 1606572 (2017).
3. J. Xu, J. Ma, Q. Fan, S. Guo, and S. Dou, *Adv. Mater.*, **29**, 1606454 (2017).
4. X. Shen, H. Liu, X.-B. Cheng, C. Yan, and J.-Q. Huang, *Energy Storage Mater.*, **12**, 161 (2018).
5. A. Eftekhari and B. Ramanujam, *J. Mater. Chem. A*, **5**, 7710 (2017).
6. B. D. McCloskey and D. Addison, *ACS Catal.*, **7**, 772 (2017).
7. M. Carboni, A. G. Marrani, R. Spezia, and S. Brutti, *Chem. - A Eur. J.*, **22**, 17188 (2016).
8. B. Adams et al., *Adv. Energy Mater.*, **5**, 1 (2015).
9. Y. Tu, D. Deng, and X. Bao, *J. Energy Chem.*, **25**, 957 (2016).
10. H. Woo et al., *Electron. Mater. Lett.*, **12**, 551 (2016).
11. S. Freunberger et al., *Angew. Chemie - Int. Ed.*, **50**, 8609 (2011).
12. C. Liu and S. Ye, *J. Phys. Chem. C*, **120**, 25246 (2016).
13. D. Zhu et al., *J. Solid State Electrochem.*, **17**, 2865 (2013).
14. M. Carboni, S. Brutti, and A. G. Marrani, *ACS Appl. Mater. Interfaces*, **7**, 21751 (2015).
15. D. Giacco, M. Carboni, S. Brutti, and A. G. Marrani, *ACS Appl. Mater. Interfaces*, **9**, 31710 (2017).
16. L. Li et al., *J. Mater. Chem. A*, **3**, 24309 (2015).
17. Z. Sadighi et al., *J. Power Sources*, **365**, 134 (2017).
18. X. Lin, J. Su, L. Li, and A. Yu, *Electrochim. Acta*, **168**, 292 (2015).
19. H. S. Jadhav et al., *J. Electrochem. Soc.*, **161**, A2188 (2014).
20. B. Sun, J. Zhang, P. Munroe, H.-J. Ahn, and G. Wang, *Electrochem. commun.*, **31**, 88 (2013).
21. D. Giacco, A. G. Marrani, and S. Brutti, *Mater. Lett.*, **224**, 113 (2018).
22. F. S. Gittleson et al., *Phys. Chem. Chem. Phys.*, **16**, 3230 (2014).
23. P. G. Imanishi, N. Luntz, and A. Bruce, *The Lithium Air Battery: Fundamentals*, Springer, New York (USA), (2014).
24. M. Carboni, A. G. A. G. Marrani, R. Spezia, and S. Brutti, *J. Electrochem. Soc.*, **165**, 1 (2018).
25. Y.-C. Lu et al., *J. Am. Chem. Soc.*, **132**, 12170 (2010).
26. K. Huang, T. Song, O. Morales-Collazo, H. Jia, and J. F. Brennecke, *J. Electrochem. Soc.*, **164**, F1448 (2017).
27. D. A. Agyeman, M. Park, and Y.-M. Kang, *J. Mater. Chem. A*, **5**, 22234 (2017).
28. D. Zhang, B. Gökce, and S. Barcikowski, *Chem. Rev.*, **117**, 3990 (2017).
29. A. De Bonis, A. Santagata, A. Galasso, A. Laurita, and R. Teghil, *J. Colloid Interface Sci.*, **489**, 76 (2017).
30. A. De Bonis, M. Sansone, A. Galasso, A. Santagata, and R. Teghil, *Appl. Phys. A Mater. Sci. Process.*, **117**, 211 (2014).
31. A. De Bonis et al., *Catal. Commun.*, **100**, 164 (2017).
32. M. D. Abràmoff, P. J. Magalhães, and S. J. Ram, *Biophotonics Int.*, **11**, 36 (2004).
33. Z. Q. Yang et al., (2008) http://link.springer.com/10.1007/978-3-540-85228-5.
34. Ľ. Pikna et al., *J. Solid State Chem.*, **212**, 197 (2014).
35. Q. Zhao, Z. Yan, C. Chen, and J. Chen, *Chem. Rev.*, **117**, 10121 (2017).
36. J. Donohue, *The structure of elements*, Wiley, New York (US), (1974).
37. C. J. Toussaint, *J. Appl. Cryst.*, **4**, 293 (1971).
38. B. Beverskog and I. Puigdomenech, *Corros. Sci.*, **39**, 969 (1997).
39. J.-G. Kim, D. L. Pugmire, D. Battaglia, and M. A. Langell, *Appl. Surf. Sci.* (2000).
40. A. Thissen et al., *Chem. Mater.*, **17**, 5202 (2005).
41. J. van Elp, H. Eskes, P. Kuiper, and G. A. Sawatzky, *Phys. Rev. B*, **45**, 1612 (1992).
42. D. Alders, F. C. Voogt, T. Hibma, and G. A. Sawatzky, *Phys. Rev. B*, **54**, 7716 (1996).
43. L. Soriano et al., *Phys. Rev. B - Condens. Matter Mater. Phys.* (2007).
44. R. J. O. Mossanek et al., *Chem. Phys. Lett.* (2011).
45. M. Lenglet, R. Guillamet, J. Dürr, D. Gryffroy, and R. E. Vandenberghe, *Solid State Commun.*, **74**, 1035 (1990).
46. M. C. Biesinger et al., *Appl. Surf. Sci.*, **257**, 2717 (2011).
47. K. S. Kim, A. F. Gossmann, and N. Winograd, *Anal. Chem.*, **46**, 197 (1974).
48. M. Brun, A. Berthet, and J. Bertolini, *J. Electron Spectros. Relat. Phenomena*, **104**, 55 (1999).
49. *Version 4.1 (National Inst. Stand. Technol. Gaithersburg)*; (2012) http://srdata.nist.gov/xps/.
50. X. Gao, Z. P. Jovanov, Y. Chen, L. R. Johnson, and P. G. Bruce, *Angewandte Chemie*, **56**, 6539 (2017).
51. K. U. Schwenke et al. *J. Electrochem. Soc.* **162**, A573 (2015).
52. P. Verma, P. Maire, and P. Novák, *Electrochim. Acta*, **55**, 6332 (2010).
53. N. Mahne et al., *Nat. Energy*, **2**, 17036 (2017).
54. J. Wandt et al., *Angew. Chemie.* **128**, 7006 (2016).
55. U. Das, K. C. Lau, P. C. Redfern, and L. A. Curtiss, *J. Phys. Chem. Lett.* **5**, 813 (2014).